


Synthetic-Ferromagnet Pinning Layers Enabling Top-Pinned Magnetic Tunnel Junctions for High-Density Embedded Magnetic Random-Access Memory

Enlong Liu,^{*,‡} Y.-C. Wu,[‡] S. Couet, S. Mertens, S. Rao, W. Kim, K. Garello, D. Crotti, S. Van Elshocht, J. De Boeck,[‡] G. S. Kar, and J. Swerts[†]
imec, Kapeldreef 75, Leuven 3001, Belgium

 (Received 16 July 2018; revised manuscript received 10 October 2018; published 26 November 2018)

Magnetic tunnel junctions (MTJs) with perpendicular magnetic anisotropy (PMA) have been developed for decades for spin-transfer-torque magnetic random-access memory. Common stack designs use a hard layer (HL) with strong PMA to pin the reference layer (RL) by forming a synthetic antiferromagnet through a thin nonmagnetic coupling layer. Compared to bottom-pinned MTJs, very limited progress has been made to top-pinned MTJs, especially on the RL pinning due to its inferior thermal robustness. Herein, an alternative stack design is proposed for top-pinned MTJs, i.e., a synthetic ferromagnet (SFM). In the SFM, the RL is coupled with the HL ferromagnetically through a coupling layer. Micromagnetic simulations predict the advantage of the SFM design to stabilize the RL at scaled critical dimension (CD), which is experimentally proven by the observation of an increased RL pinning field on the device level. Because of the RL stray field acting on the free layer (FL), a compensation magnet (CM) is inserted below the FL to form a top-pinned MTJ stack without compromising magnetotransport properties. Devices with centered FL switching loops can be obtained after a two-step field setting. The stray field of CM has limited impact on the RL due to the large distance in between, thus keeping the RL's pinning field larger than 150 mT down to devices with 20-nm CD. Finally, current switching is realized in devices with SFM and CM, showing critical current density around 5–8 MA/cm² and an averaged thermal stability as high as 50. Thus, the SFM pinning layer design shows great potential in stabilizing top-pinned devices and paves the way for multiple future spintronic applications requiring a top-pinned stack design.

DOI: [10.1103/PhysRevApplied.10.054054](https://doi.org/10.1103/PhysRevApplied.10.054054)

I. INTRODUCTION

Spin-transfer-torque magnetic random-access memory (STT MRAM) has drawn interest for decades as a candidate for the next-generation memory to replace static RAM and/or dynamic RAM, due to its scaling potential and nonvolatility [1]. As the key component, magnetic tunnel junctions (MTJs) have been under development to fulfill the requirements of memory applications, such as fast response speed, low power consumption, long data-retention time, and high thermal robustness [2]. Recently, MTJs with perpendicular magnetic easy axis (PMTJs) have shown all of the desired properties mentioned above at scaled critical dimension (CD) [3,4]. To work properly as a memory cell, one PMTJ is composed of several functional layers. The free layer is the data-storage layer, whose magnetic moment can be switched by the writing current. On the other hand, the reference layer should stay fixed

during the FL switching to define data states from high or low junction resistance. The PMTJ studies nowadays are mainly based on a Co-Fe-B/MgO/Co-Fe-B tunnel junction after the discovery of its interfacial perpendicular magnetic anisotropy (PMA), which can provide high tunnel magnetoresistance (TMR) and realize fast switching [5,6]. To keep the moment in the reference layer fixed, the common solution is to build a synthetic antiferromagnet (SAF), where the reference layer is antiferromagnetically coupled through a thin Ru or Ir spacer with another functional layer possessing strong PMA, i.e., the pinning layer or hard layer [7–10]. By doing so, the pinning field of the reference layer can be increased and well separated from the coercive field (H_c) of the FL to avoid switching disturbance. Another advantage of SAF design is the compensation of the stray field from the reference layer by the hard layer, and hence the offset field of the free layer is reduced to get rid of switching asymmetry.

According to the position of SAF and the tunnel junction, both bottom-pinned and top-pinned stacks are designed, as shown in Figs. 1(a) and 1(b), respectively. Most research focused on bottom-pinned stacks because of its stability after postannealing to meet the back-end-of-line (BEOL) compatibility requirements in CMOS flows

*enlong.liu@imec.be

†johan.swerts@imec.be

‡Department of Electrical Engineering (ESAT), KU Leuven, Leuven 3001, Belgium.

[11–14]. However, the working principle of top-pinned MTJs fits better with the asymmetry of driving current from planar or FinFET transistors [15]. Besides, the top-pinned stack design has the potential to outperform its bottom-pinned counterpart from the free layer point of view, as new materials with large PMA and low damping are researched to increase the free-layer thermal stability (Δ) and spin-torque efficiency in PMTJ devices after scaling down to sub 20 nm. Potential materials such as $L1_0$ -FePt [16,17], $D0_{22}$ -Mn₃Ge [18,19], and Heusler alloys [20] require crystalline seeds as templates to obtain the desired crystalline phase. A seed cannot be done in bottom-pinned stacks since the free layer needs to be deposited on top of the MgO barrier. In top-pinned stacks, the seed choices are flexible and hence it is more friendly for free-layer material studies and integration. Moreover, many advanced spintronic applications such as memory based on domain wall motion and spin-orbit-torque (SOT), rely on a top-pinned design, which is preferred from a patterning perspective [21,22]. The key issues of the top-pinned SAF stack design is the weak reference-layer pinning field and the insufficient thermal robustness of the SAF at high temperature [23]. Indeed, the former issue is general in SAF design, because it is caused by the magnetic moment in the hard layer aligned antiparallel with the reference layer, whose stray field generated in devices destabilizes the reference layer. This reference layer destabilization does not occur in the bottom-pinned SAF design. Because the exchange coupling is large enough, there remains a sufficient margin even when the stray field of the hard layer lowers the reference-layer pinning field. In the top-pinned SAF design, however, the exchange coupling is lower due to its worse crystallinity, leading to destabilization of the reference layer. The insufficient thermal robustness is caused by the interdiffusion between the hard layer and the MTJ in the stack after annealing [24]. No solution for top-pinned SAF stacks has been identified to solve the reference-layer switching instability on devices and the incompatibility to postannealing above 375°C until our recent study introduced a synthetic-ferromagnet (SFM) design [24]. The SFM consisted of a hard layer and a reference layer that are ferromagnetically coupled via a nonmagnetic spacer.

In this paper, we first describe the material choices and their interactions in the SFM design. Next, the detailed characterization and in-depth understanding of the magnetic behavior and switching properties of the top-pinned SFM stack design on both blanket and device level is discussed. Section II describes the experimental details, including material and device fabrication. Section III introduces the concept of SFM starting from micromagnetic simulations, which confirms the improvement of the pinning effect to the reference layer by the hard layer when the magnetic moments are aligned parallel. To realize the parallel alignment in the SFM, the interlayer exchange

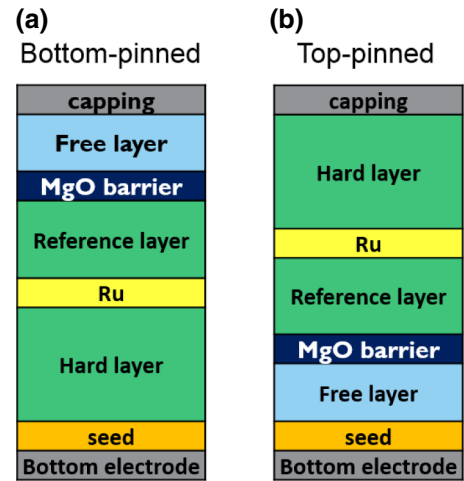


FIG. 1. Schematic drawings of conventional PMTJ stacks with the SAF design: (a) bottom-pinned stack; (b) top-pinned stack. In the SAF design, Ru provides antiferromagnetic coupling between the reference and hard layers.

coupling of the Ru spacer, especially in the ferromagnetic coupling range, is investigated. Afterwards, we discuss the magnetic and electrical properties of top-pinned stacks with SFM design. In Sec. IV, a compensation magnet (CM) is introduced for stray field compensation. The impact of the CM on the offset field of the free layer and on the pinning field of the reference layer is discussed. Finally, the current switching is demonstrated in the device with SFM design and CM, showing current density 5–8 MA/cm², and Δ as high as 50.

II. EXPERIMENTS

The blanket samples of top-pinned MTJs using [Co/Pt] multilayers as the hard layer in the SFM and as CM are deposited *in situ* at room temperature on 300-mm Si wafers with the bottom electrode. The bottom electrode consists of TaN(5)/CuN(50)/TaN(3)/CuN(50)/TaN(40) (units in nm hereafter), and is smoothed by chemical-mechanical polishing. Both the bottom electrode and stacks above are deposited by physical vapor deposition in a Canon Anelva EC7800 cluster. The chamber design allows wedges to be deposited to study the impact of the thickness of a single layer in the top-pinned MTJ stacks. The free layer is the typical dual-MgO free layer, i.e., MgO(0.5)/Co-Fe-B(0.9)/Ta(0.4)/Co-Fe-B(1.0)/MgO(1.0) system. The reference layer consists of Co-Fe-B(1.3)/Ta(0.4)/Co(1.2), and the hard layer is composed of Co(0.6)/Pt(0.8)/[Co(0.3)/Pt(0.8)]₆ [23]. All wafers receive annealing in a 1-T magnetic field at 400°C for 30 min, while those for device fabrication receive the same magnetic-field annealing but at 375°C for 30 min. All annealing processes are conducted in a TEL-MSL MRT5000 batch-annealing system. The perpendicular hysteresis loops of the blanket

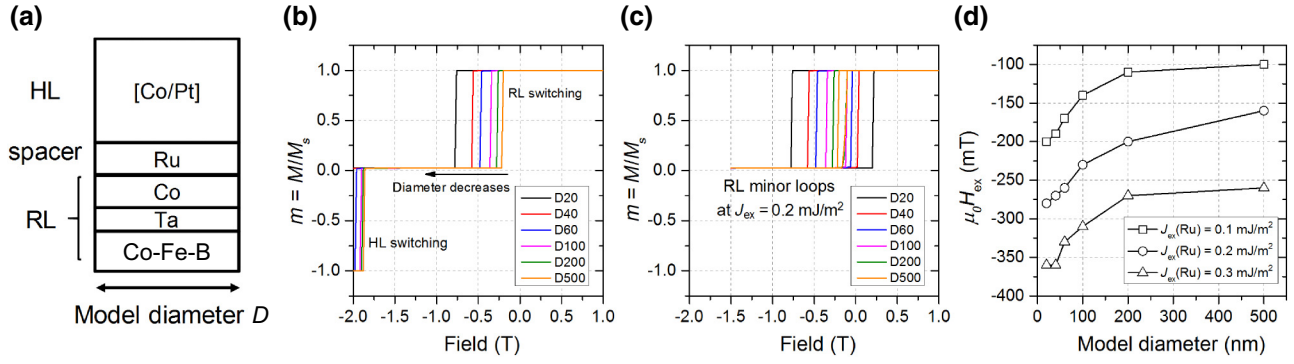


FIG. 2. (a) Model used for SFM switching simulations. (b) Simulated switching of the reference layer (RL) and the hard layer (HL) with external field. The RL switches before the HL. As the model diameter decreases, the pinning field of RL increases. (c) Minor loops of RL from the same models as in (b). Simulations in (b),(c) use $J_{\text{ex}} = 0.2 \text{ mJ/m}^2$. (d) $\mu_0 H_{\text{ex}}$ of RL in SFM models derived from (b). The H_{ex} of RL in the SFM model increases as the diameter decreases and also as J_{ex} increases.

samples are measured with a Microsense vibrating sample magnetometer (VSM), while the TMR and resistance-area product (RA) measurements are done via the current-in-plane tunneling method (CIPT) using a Capres setup [25]. For the electrical properties studies, the patterning of top-pinned MTJs stack into circular devices with various diameters from 500 nm down to sub 20 nm is done by UV lithography and ion-beam etching. To align the magnetic moment in the SFM and CM antiparallel, a two-step field setting is conducted. First a 2-T field is applied, and followed by a second magnetic field in the opposite direction whose value depends on the device size.

The Object-Oriented Micromagnetic Framework (OOMMF) project is used for the simulations [26].

III. TOP-PINNED MTJS WITH SFM DESIGN

A. Enhanced pinning in the SFM design: micromagnetic simulations

As mentioned above, a significant decrease of reference-layer pinning field in top-pinned devices with SAF is observed, which can lead to backhopping events in the reference layer and increase the write-error rate. It is attributed to the antiparallel alignment between the reference layer and the hard layer, which causes the reference-layer destabilization after patterning due to the stray field from the hard layer. Unlike the SAF design, however, the proposed SFM design consists of a reference layer and a

parallel aligned hard layer. The stray field in devices from the hard layer (reference layer) is expected to be aligned along the direction of the magnetic moment in the reference layer (hard layer), and hence should strengthen the parallel coupling, especially in devices at small CD where the stray field becomes larger.

To confirm the above hypothesis, micromagnetic simulations are conducted to predict the switching behavior of SFM after patterning. Figure 2(a) illustrates the SFM model used in simulations. A detailed model is used for the reference layer, which consists of Co-Fe-B, Ta interlayer and thin Co layer [23]. The input parameters of each layer are listed in Table I. The M_s of each layer are derived from previous work [27]. K_U means the uniaxial anisotropy energy density of each layer. A_{ex} is the exchange stiffness of each layer. The coupling constant (J_{ex}) provided by Ta in the reference layer remains unchanged [28,29]. In the simulation, we focus on the impact of J_{ex} from the Ru spacer on the exchange field of the reference layer in the SFM, i.e., H_{ex} and its size dependence. The moment-field (M - H) loops are plotted for models with decreasing diameters in Fig. 2(b). A two-step switching profile is observed: the reference layer switches firstly due to its lower PMA, then followed by the hard layer. If the model diameter decreases, the switching field of the reference layer increases as indicated in Fig. 2(b). The reason for the increase is twofold. Firstly, it is clear in Fig. 2(c) that the H_c of the reference layer increases as the model

TABLE I. Input parameters used in the micromagnetic simulations for the SFM design shown in Fig. 2(a).

	Thickness (nm)	K_U (J/m ³)	M_s (kA/m)	A_{ex} (pJ/m)	J_{ex} (mJ/m ²)
[Co/Pt]	8	6e5	450	10	NA
Ru spacer	1.2	0	0	0	0.1, 0.2, 0.3
Co	1.2	12.5e5	1200	15	NA
Ta	0.4	0	0	0	0.1
Co-Fe-B	1.2	10e5	1100	20	NA

diameter decreases, which contributes to the increase of the reference-layer switching field shown in Fig. 2(b). Secondly, the hard-layer stray field in SFM design is also stabilizing the reference layer due to the parallel alignment of the magnetic moments in all simulations. And the stray-field value increases as the model diameter reduces. To clarify the reference-layer switching-field dependence on the hard layer, the coupling strength (H_{ex} here) should be focused. It combines the intrinsic ferromagnetic coupling strength from the Ru spacer and the extrinsic stray field from the hard layer. From the minor loops of the reference layer in Fig. 2(c), the H_{ex} are derived and plotted in Fig. 2(d). Indeed, H_{ex} increases with J_{ex} at a fixed model diameter, and with the decreasing model diameter at fixed J_{ex} . The simulations confirm that the reference layer can be well pinned by the hard layer in the SFM design due to the ferromagnetic coupling and the increasing stray field from the hard layer at decreasing CD.

B. Spacer study in the SFM design: ferromagnetic coupling

As mentioned in the introduction, both top-pinned and bottom-pinned PMTJs at present mainly use a SAF design, where antiferromagnetic coupling is required. Typical spacers to provide antiferromagnetic coupling are Ru and Ir, based on Ruderman-Kittel-Kasuya-Yosida (RKKY) coupling theory, as illustrated schematically in Fig. 3(a) [30]. To our knowledge, however, no report studying the ferromagnetic coupling in the context of the pinning layer and its thermal robustness exists. Therefore, the coupling property of a Ru spacer is studied to establish a SFM pinning layer. The following stack is used Ru(3)/[Co(0.3)/Pt(0.8)]₃/Co(0.6)/Ru(t_{Ru})/Co(0.6)/[Pt(0.8)/Co(0.3)]₃/Ru(3), with t_{Ru} Ru spacer thickness [see the inset of Fig. 3(a)].

The antiferromagnetic coupling provided at $t_{\text{Ru}} = 0.4$ nm and $t_{\text{Ru}} = 0.85$ nm [the first and second peak, respectively, in the positive area in Fig. 3(a)] decreases with

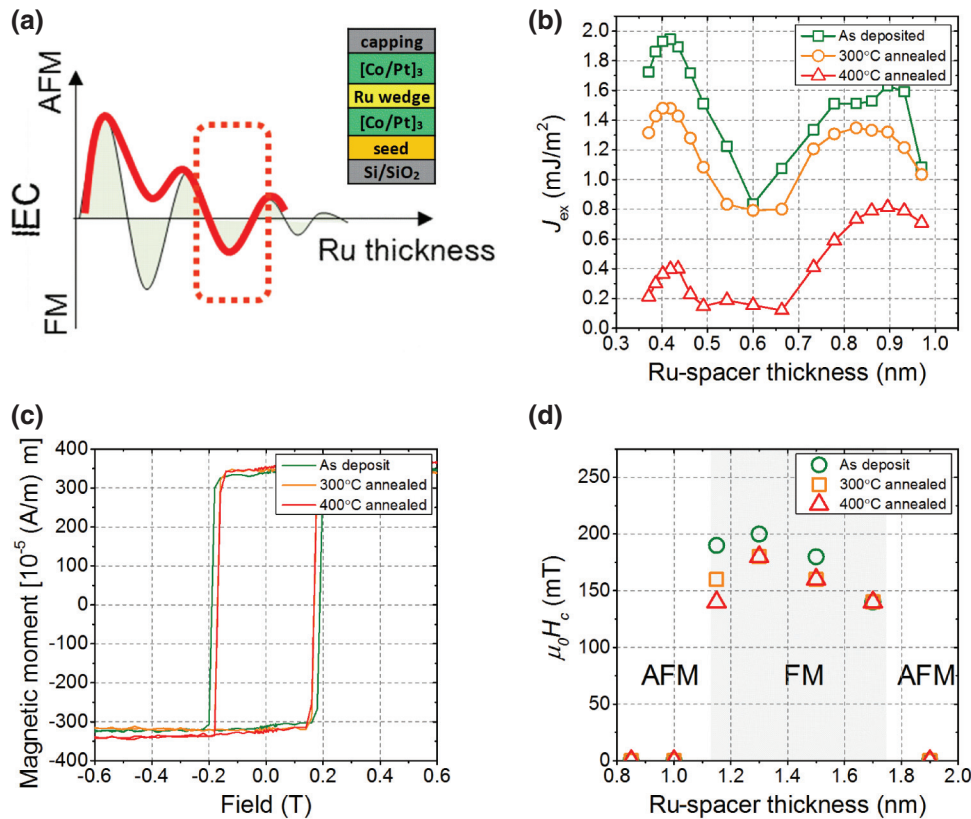


FIG. 3. (a) Schematics of RKKY coupling behavior of the Ru spacer. Black solid curve schematically represents the analytical result from quantum-interference theory [30]. The red solid curve reflects the observed results in experiments. To apply in SFM, the thickness range with ferromagnetic coupling is focused on, as emphasized by the red dashed box. The inset is the stack used for the interlayer exchange coupling (IEC) study of the Ru spacer. (b) Antiferromagnetic J_{ex} as a function of Ru spacer thickness in (a) for the as deposited, after 300°C annealing, and after 400°C annealing, respectively. The reduction of J_{ex} after annealing is more dramatic for the thinner Ru spacer. (c) VSM loops of samples with the 1.3-nm Ru spacer providing ferromagnetic coupling for the as deposited, after 300°C annealing, and after 400°C annealing, respectively. (d) Coercive field of the samples as a function of the Ru thickness range with ferromagnetic (FM) coupling. For Ru thickness with antiferromagnetic (AFM) coupling, use $\mu_0 H_c = 0$ T artificially. Ferromagnetic coupling strength reaches the largest at 1.3 nm Ru due to the largest $\mu_0 H_c$.

postannealing. After 400°C annealing, the J_{ex} drops to quarter of the as-deposited value for the 0.4-nm Ru spacer, and half for the 0.85-nm Ru spacer. The PMA of the stack degrades as well (VSM not shown). As a comparison, Fig. 3(c) shows the hysteresis loops of the sample with $t_{\text{Ru}} = 1.3$ nm after different annealing treatments. Perfect PMA is kept up to 400°C annealing with a minor change in H_c . Unlike for antiferromagnetic coupling, the calculation of ferromagnetic J_{ex} from the magnetization loops is not possible since only a single switching event occurs. Therefore, the H_c is used as the representative of ferromagnetic coupling strength in Fig. 3(d) in all samples with various Ru spacer thicknesses. A clear peak is observed in H_c at a Ru spacer thickness of 1.3 nm, indicating the spacer thickness with the largest ferromagnetic coupling strength. Note that the H_c remains unchanged after 400°C annealing, meaning that ferromagnetic coupling survives and stays stable in contrast to the antiferromagnetic coupling at the first and second peak. The thick Ru with ferromagnetic coupling will be the key layer of the SFM design and plays a vital role for the annealing stability of the devices.

C. Reference-layer switching field in SFM: from blanket to devices

Using the interlayer exchange coupling from the Ru spacer, a top-pinned MTJ stack with the SFM pinning layer is deposited, which is shown schematically in Fig. 4(a). The Ru thickness has been varied around its peak of ferromagnetic coupling derived from the simple stack study in the previous section. Figure 4(b) shows the VSM perpendicular loop of the stack when the Ru spacer is 1.3-nm thick. Clear sharp switching of all functional layers is observed, with the TMR up to 170%, and RA equals 9.5 $\Omega \mu\text{m}^2$. Unlike in the SAF where the reference layer switches before external field changes direction, the reference layer switches just before the hard-layer switching field in SFM design, which is attributed to the

ferromagnetic coupling through the 1.3 nm Ru spacer. If the thickness of the Ru spacer changes, the TMR, switching field of the reference layer and the hard layer of the stack will be influenced, as shown in Fig. 4(c). The TMR increases slightly, which is due to less Pt interdiffusion in SFM blocked by the thicker Ru spacer [24]. The switching field (or pinning field) of the reference layer reaches maximum when the Ru spacer is 1.3 nm, while that of the hard layer is at the minimum correspondingly. This phenomenon can be briefly explained using a coupled system between a soft magnet (reference layer) and a hard magnet (hard layer). The ferromagnetic coupling in between strengthens the soft magnet and hence requires large field to switch, while the ferromagnetic coupling in turn *softens* the hard magnet and reduces its switching field. Results above indicate that the ferromagnetic coupling is the largest at the 1.3-nm Ru spacer, which is in agreement with the simplified stack results [see Fig. 3(d)]. Due to the high coercive field of the hard layer leading to distinct switching fields of the reference layer and the hard layer, the coupling strength J_{ex} can be calculated in this partial stack case using

$$J_{\text{ex}} = \mu_0 H_{\text{ex}}^{\text{RL}} M_s^{\text{RL}} t, \quad (1)$$

which is normally used for antiferromagnetic coupling strength calculation [31]. In Eq. 1, M_s^{RL} is the magnetization of the reference layer, t is reference-layer thickness, and $\mu_0 H_{\text{ex}}^{\text{RL}}$ is the exchange field of the reference layer. Here the switching field of the reference layer is used as $\mu_0 H_{\text{ex}}^{\text{RL}}$ due to the negligible coercivity of the reference layer [red minor loop in Fig. 4(b)]. The results are plotted in Fig. 4(d) as a function of Ru thickness. J_{ex} is 0.2 mJ/m² at Ru 1.3 nm, which is sufficient to couple the reference layer to the hard layer to form a SFM. Furthermore, this SFM design at 400°C shows an advantage in maintaining PMA and TMR, therefore, clearly outperforming

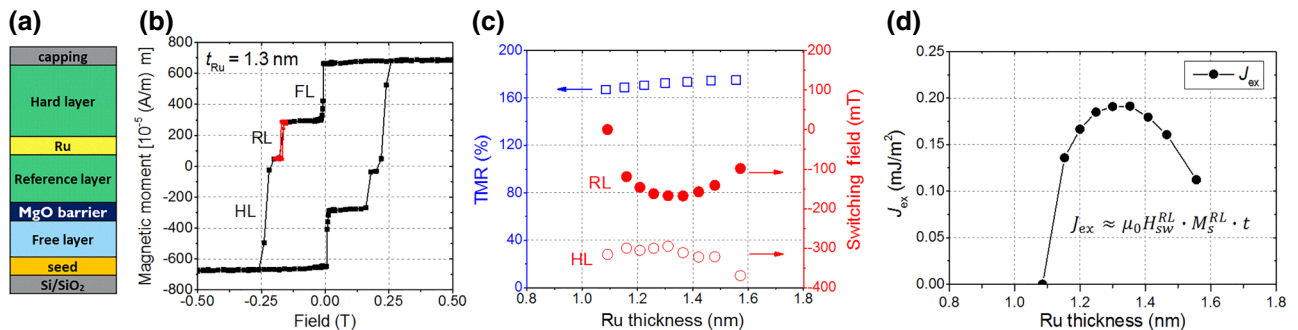


FIG. 4. (a) Schematic of top-pinned MTJ stack with SFM design (b) VSM loop of the top-pinned MTJ blanket sample with a 1.3-nm Ru spacer in SFM after 400°C annealing. The minor loop of RL switching is plotted as the red loop. This stack provides 170% in TMR and 9.5 $\Omega \mu\text{m}^2$ in RA. (c) TMR and the switching field of the reference layer and the hard layer as a function of Ru-spacer thickness from the stack in (a). The minus sign in the switching field only indicates the direction of the external field. The absolute values should be used for calculation. (d) Exchange coupling constant (J_{ex}) as a function of Ru-spacer thickness.

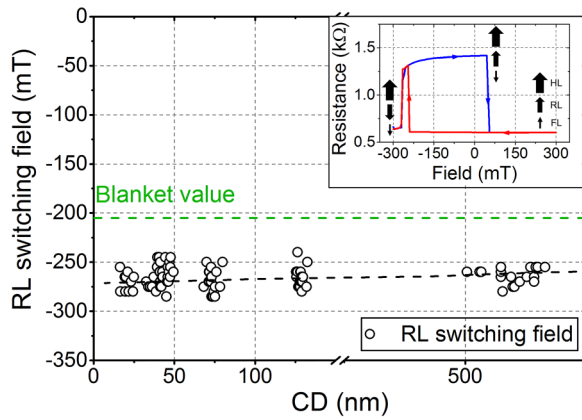


FIG. 5. The reference-layer (RL) switching field in devices as a function of CD. The blanket value is indicated as the green dashed line. The black dashed line is a guide to the eyes. The inset is a typical R - H loop of one device with 130-nm CD. The coercive field of the reference layer is small, which is probably due to the loss of its PMA during patterning.

its SAF counterpart, where a severe PMA and TMR loss is observed at 400°C [23].

The stack in Fig. 4(a) is patterned into devices with various CD to validate experimentally the advantage of SFM shown by simulations (see Secs. III A). The resistance-field (R - H) loops are measured to show the free-layer and reference-layer switching, as indicated in the inset of Fig. 5. The H_c of the reference layer is low in devices, which can originate from PMA loss during the patterning process, but its pinning field becomes larger than on blanket samples. However, the pinning field of the reference layer shows almost no dependence on the CD of the devices, which deviates from the simulation results in Fig. 2(d). It is due to the presence of the free-layer stray field in experiment, which is ignored in the simulations. Actually, the pinning field of the reference layer on devices is determined not only by the hard layer but also by the free layer. As shown in the inset of Fig. 5, the magnetic moment in the hard layer and the free layer are antiparallel when the reference layer switches. The stray field from the hard layer onto the reference layer is partially canceled out by that from the free layer, whose value also increases with decreasing device CD. As a result, the net stray field on the reference layer shows really no CD dependence (refer to the explanation of Fig. 9(c) in Secs. IV B). Despite the negative contribution from the free-layer stray field, the pinning field of the reference layer is larger than on blankets. It means that the hard layer plays the dominant role in pinning the reference layer in the SFM design, especially after patterning. This confirms that the pinning field of the reference layer can benefit from the scaling of top-pinned MTJ devices with the SFM design due to the parallel alignment with the hard layer.

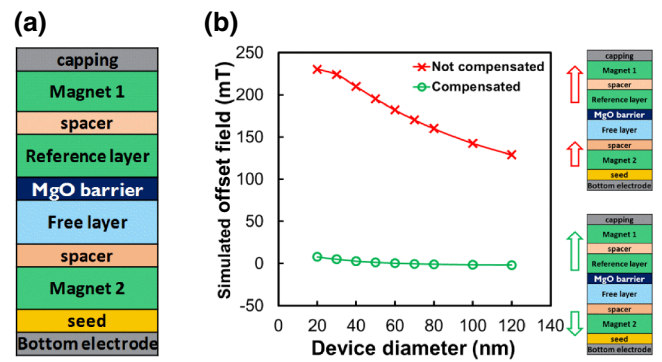


FIG. 6. (a) Schematic drawings of a PMTJ stack with two magnets sandwiching the free layer. (b) Simulated offset field of the free layer in the stack design in (a). Low offset field can be achieved if the two magnets are aligned antiparallel.

IV. TOP-PINNED MTJS WITH SFM AND COMPENSATION MAGNET

The top-pinned MTJs with the SFM pinning layer studied above maintain high TMR and PMA in all layers, and the pinning field of the reference layer benefits from parallel alignment with the hard layer after patterning. However, the switching asymmetry of the free layer will be large in the device, as shown in the inset of Fig. 5. Unlike SAF, there is no compensation in the stray field between the reference layer and the hard layer in SFM, which leads to a very large free-layer offset field. Actually, the stray-field compensation in the SFM design can be realized by inserting another magnet in the stack with the magnetic moment aligned antiparallel to the SFM, as proposed by Iba *et al.* [32]. It is a stack design with two magnets sandwiching the free layer, as illustrated in Fig. 6(a). In this way, the offset field of the free layer can be kept low and independent of device dimensions once the two magnets are aligned antiparallel, as shown by simulation results in Fig. 6(b).

In this work, the SFM in Fig. 4(a) functions as the reference layer and spacer and Magnet-1 in Fig. 6(a). And a $[\text{Co}(0.5)/\text{Pt}(0.3)]_6$ multilayer is inserted below the stack as Magnet 2, namely the compensation magnet (CM), to cancel out the stray field from the SFM. Its structure and perpendicular hysteresis loop are illustrated in Fig. 7(a). The insertion of CM has no impact on the free-layer switching [see the inset in Fig. 7(a)] and the PMA of each functional layer in the full stack is maintained after annealing. Besides, there is no impact from the CM to the magnetotransport properties of the tunnel junction. As shown in Fig. 7(b), the TMR and RA are identical to the stack without CM. Thus, a top-pinned stack with SFM design and CM is successfully obtained with TMR around 160% and maintains PMA in all functional layers. That stack is patterned into devices with various dimensions for the study of the impact of the CM on the free-layer offset field and reference-layer pinning field.

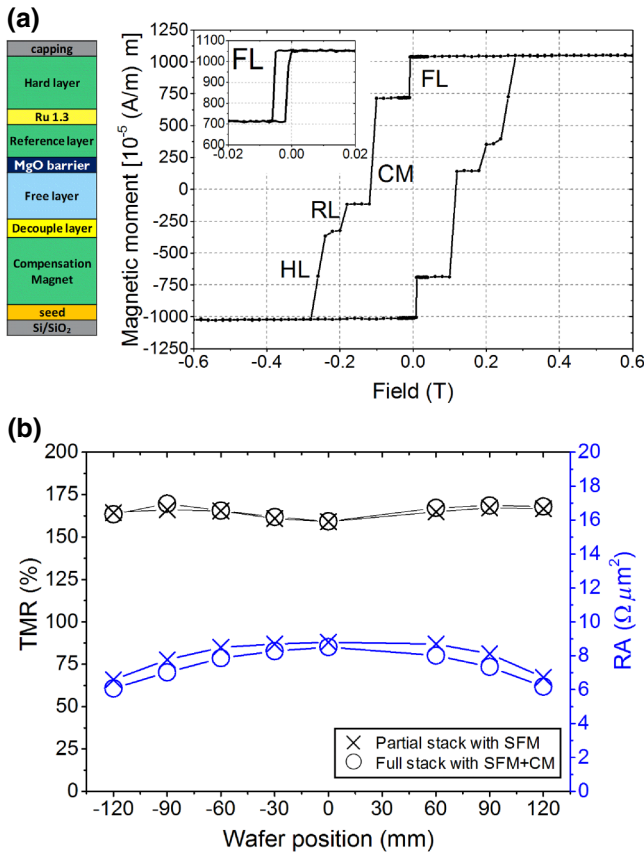


FIG. 7. (a) Stack structure and perpendicular hysteresis loop of the top-pinned SFM stack with a CM. The decouple layer is to separate the free layer and CM magnetically, and to serve as a seed layer for free-layer growth. The inset indicates that the PMA of the free layer is not influenced by the CM. (b) TMR and RA line scan on a full wafer for a SFM stack with CM (open circles) and without CM (crosses), showing the CM does not affect the TMR and RA performance.

A. Free layer with low offset field

As mentioned above, only when the CM and SFM are aligned antiparallel can a low offset field be obtained. Thus, a two-step field setting is needed to flip the SFM part or the CM for stray-field compensation. To demonstrate the free-layer offset-field control by field setting, the *R-H* loop from a single device in uncompensated (red loop) and compensated (green loop) cases are shown in the inset of Fig. 8. For this device, a 2-T field is firstly applied to align both SFM and CM for the uncompensated case, and then a 0.55 T in the opposite direction to align the CM antiparallel with the SFM for the compensation case. Obviously, the PMA of the free layer remains perfect after patterning, which leads to the sharp switching in the loops. The offset field of the free layer is quite large (red loop) when the CM and SFM are aligned parallel in the uncompensated case. In contrast, the free-layer loop becomes centered (green loop) if the second magnetic field in the opposite direction is

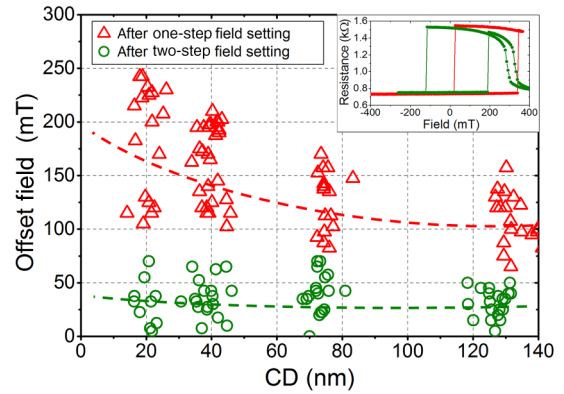


FIG. 8. Free-layer offset field in devices with various CD: after one-step field setting (red triangles) and after two-step field setting (green circles). Dashed lines are guides for the eyes. The inset is one example of the *R-H* loop for devices with 130-nm CD, showing that the control of the free-layer offset field can be realized with two-step field setting and low offset field can be obtained.

applied, after which the CM is flipped to align antiparallel with the SFM as the compensated case.

However, the derivation of CD dependence of the free-layer offset field is not straightforward. The issue stems from the variation in the H_c of SFM and CM in devices with different CDs. The inverse magnetic field in the second step may not flip the CM in all devices with various CDs. Therefore, multiple wafers with the same stack have been fabricated into devices. And two-step field settings with different inverse magnetic field (0.5, 0.55, 0.6 T) in the second step have been conducted trying to achieve a centered free layer in devices with different CDs. Using this method, sufficient statistics of the free-layer offset field can be obtained, and hence its device CD dependence is derived and summarized in Fig. 8. The free-layer offset-field values from the uncompensated case are from one device wafer. The offset field increases with decreasing device diameter when the CM and the SFM are parallel, which is in agreement with simulations [see Fig. 6(b)]. After the two-step field setting, the offset field of each device can be controlled to be around 50 mT and below with almost no size dependence, even for devices down to 20 nm as expected from Fig. 6(b). Although distributions are observed in device CD and offset field, which is caused by the patterning nonuniformity, the difference in the free-layer offset field in uncompensated and compensated cases is obvious. It is then concluded here that the control of the offset field of the free layer with antiparallel aligned SFM and CM is realized, and the centered free-layer switching is obtained in devices down to 20 nm.

Although the FL offset field after two-step field setting in Fig. 8 is still significant (< 50 mT), it can be solved by dedicated designs of the HL and the CM. One way is to vary the magnetization in the two parts. To reduce

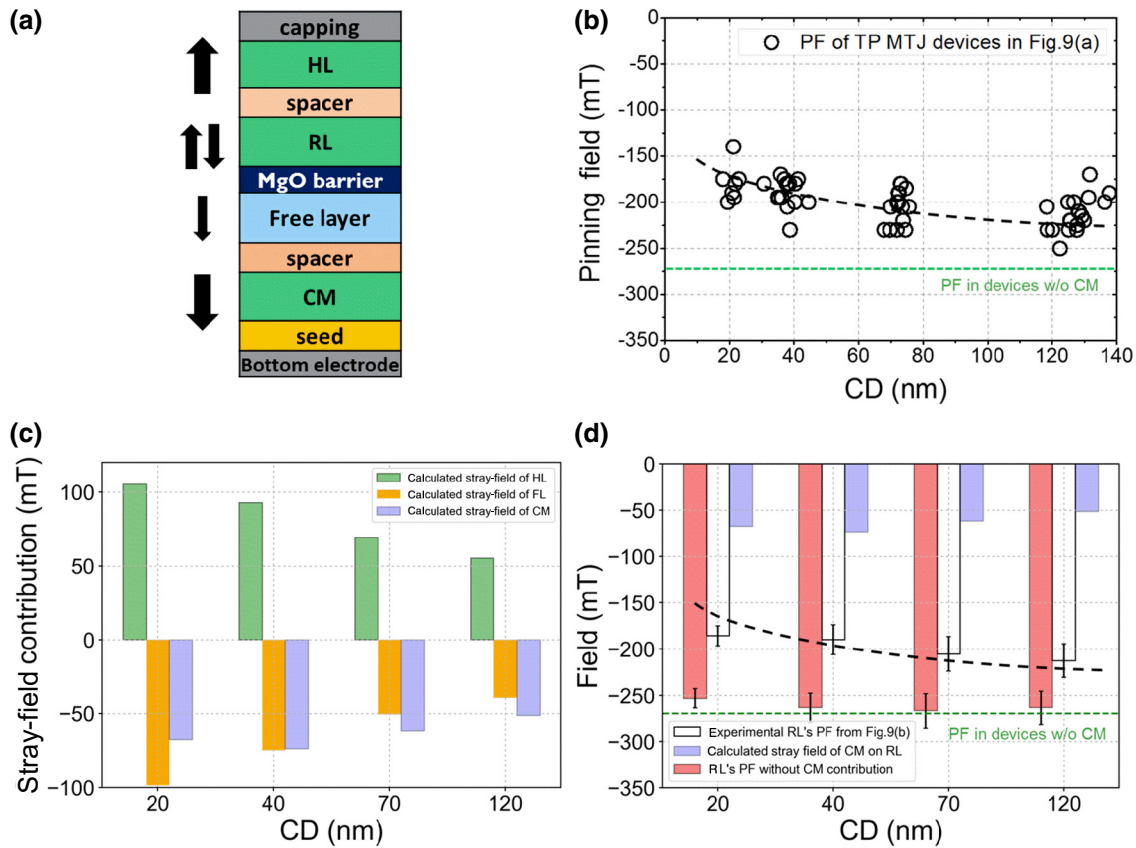


FIG. 9. (a) Schematic of the stack with SFM and CM, and its magnetization configuration. The switching of the reference layer (RL) happens with the hard layer (HL) aligned antiparallel with the free layer (FL) and CM. (b) The pinning field (PF) of RL as a function of CD. Each data point is from an individual device. (c) Calculated stray-field contribution on the RL switching from HL, FL, and CM. Positive values stabilize the RL, negative values destabilize. (d) The experimental pinning field from (b) (black hollow bars), simulated stray-field contribution from the CM [blue solid bars from (c)] and their sum (red solid bars). Black dashed lines are guides for the eyes. Green dashed lines indicate the pinning-field value from devices without CM taken from Fig. 5.

positive offset field, either increasing M_s in the hard layer or decreasing M_s in the CM can work. Another way is to increase the thickness of the decouple layer to reduce the stray field from the CM. With the two options above and the help of micromagnetic simulations, zero-offset FL switching in patterned devices can be expected in future work.

B. Impact of CM on the reference layer: limited reduction in pinning field

As discussed in Secs. III A, the advantage of SFM over SAF lies in the stabilization of the reference layer after patterning. However, the stray field of CM will also influence the reference layer, when the CM is aligned antiparallel to the SFM. Figure 9(a) shows that the switching of the reference layer happens when the magnetic moment in the hard layer aligns antiparallel with that in the free layer and CM. Reduction of the reference-layer pinning field in devices with SFM and CM is observed in Fig. 9(b), although the

pinning field stays above 150 mT in devices with down to 20-nm CD. Note that in Fig. 5, the data from the top-pinned SFM without CM show an increasing trend of reference-layer pinning field with decreasing model diameter, but in the devices with CM the opposite trend is observed. Figures 9(c) and 9(d) reveal the reason for decreasing the pinning field in SFM design. Figure 9(c) visualizes the contributions from the free layer, hard layer and CM to the stray field acting on the reference layer, as calculated using micromagnetic simulations, based on the configuration in Fig. 9(a). The stray-field values from the hard layer stabilize the reference layer, while the free layer and CM destabilize it. Obviously, the increasing deviation of the pinning field from the values in devices without CM is attributed completely to the stray field from CM, as shown in Fig. 9(d) after the compensation (blue bar plus the white bar). It is reasonable since the only difference in the magnetic configuration of the stacks in Figs. 9(a) and 4(a) is the insertion of the CM and its antiparallel alignment with the SFM. It is also noticed that the presence of CM and its

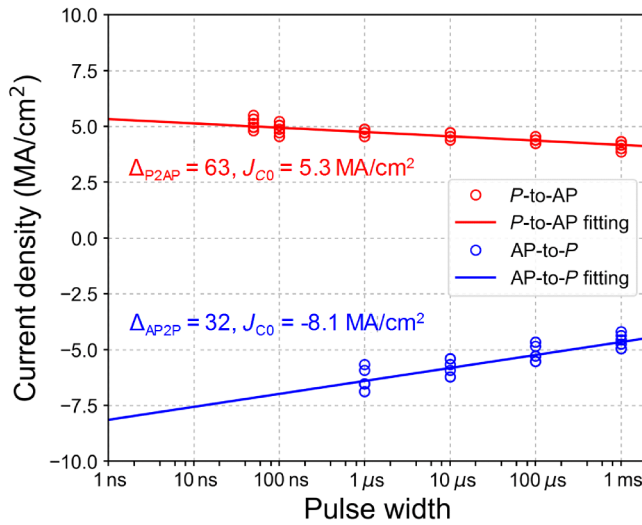


FIG. 10. Current pulse switching of a 57-nm CD device with SFM and CM design. Both antiparallel to parallel (AP-to-P) and P-to-AP switching can be realized. The fitting provides the Δ and critical switching-current density at 1-ns pulse width. The difference between the Δ of AP-to-P and P-to-AP may come from the nonperfect-centered free layer.

antiparallel aligned moments contribute more negatively to the pinning field of the reference layer as device CD decreases, but the influence is limited because the CM is positioned a few nanometers away from the reference layer. As such, the top-pinned SFM and CM design can still keep the stability of the reference layer when the CM is aligned antiparallel to bring low offset field in the free layer.

Notice that the simulated stray-field contributions from the hard layer and the free layer in Fig. 9(c) can also explain the observed size independence of the reference-layer switching field in Fig. 5. Since no CM is implemented in the stack for reference-layer-switching measurement in Fig. 5, only the hard layer and the free layer contribute to the stray-field impact on the reference layer. After calculations, the net contribution from the hard layer (green bars) and the free layer (brown bars) is independent on device size (figure not shown). Hence, the presence of the field from the free layer is confirmed as the reason why the switching field of the reference layer is not increased for smaller CD in Secs. III C.

C. Current switching demonstration

When SFM and CM are aligned antiparallel, a centered free layer and stable reference layer with large pinning field can be achieved. dc current switching is realized in devices down to 20–30 nm reported previously [24]. Herein, the current pulse switching is demonstrated, as shown in Fig. 10. The dependence of the switching-current

density on the pulse width follows

$$J(\tau) = J_{c0} \left[1 - \frac{1}{\Delta} \ln \left(\frac{\tau}{\tau_0} \right) \right], \quad (2)$$

where Δ is the thermal stability as mentioned above, τ is the pulse width, τ_0 is the inverse of the attempt frequency taken as 1 ns, J_{c0} is the critical current density for switching at 1-ns pulse width [33]. The fitting of experimental results with Eq. 2 provides Δ for both switching sides. Δ is larger in parallel to antiparallel (P-to-AP) than AP-to-P, because the free-layer switching loop is not perfectly centered in this device, which favors the parallel state. Overall, an averaged Δ around 50 is achieved with TMR of 115%. On the other hand, it is noticed that the critical switching current is larger in AP-to-P than P-to-AP. Thus, the AP-to-P switching at short pulse width requires high voltage and would cause dielectric breakdown. This abnormality is still under study.

V. CONCLUSIONS

To solve the destabilization of the reference layer in conventional top-pinned PMTJ devices and its inferior thermal robustness, an alternative pinning layer design is proposed in this paper, i.e., the synthetic-ferromagnet design, where the reference layer and the hard layer are aligned parallel. Micromagnetic simulations show the stabilization of the reference layer in the synthetic-ferromagnet structure due to the parallel alignment with the hard layer, especially in small dimensions. To realize the synthetic-ferromagnet design, ferromagnetic coupling between the reference layer and hard layer through a Ru spacer and its annealing stability is studied. With a 1.3-nm-thick Ru spacer, a synthetic-ferromagnet pinning layer with a parallel aligned reference layer and hard layer is achieved in a top-pinned MTJ stack, whose reference-layer pinning effect is stronger in devices than in blankets. The emerging offset-field issue in the free layer due to the large stray field from the synthetic-ferromagnet pinning layer can be solved by inserting a compensation magnet in the stack. Simulations reveal that low free-layer offset field can be obtained when the compensation magnet and synthetic ferromagnet are aligned antiparallel. Indeed, low offset field in the free layer with device CD independence is achieved after the insertion of the compensation magnet and proper field setting for antiparallel alignment with the synthetic ferromagnet. Moreover, the impact of the compensation magnet to reference-layer stability is proven as limited due to the long distance between the compensation magnet and reference layer. Thus, both centered free-layer switching and the stable reference layer can be obtained at the same time in top-pinned MTJ devices down to 20 nm. The current pulse switching is also demonstrated in a 57-nm CD device with critical switching-current density around

5–8 MA/cm² and an averaged thermal stability around 50. Finally, the synthetic-ferromagnet design with a compensation magnet results in robust top-pinned PMTJ devices compatible with high-temperature annealing, which paves the way for using the top-pinned stack design in various spintronic applications.

ACKNOWLEDGMENTS

This work is supported by IMEC's Industrial Affiliation Program on STT MRAM devices.

-
- [1] The International Technology Roadmap for Semiconductors (2015), <http://www.itrs2.net>.
- [2] T. Kishi, H. Yoda, T. Kai, T. Nagase, E. Kitagawa, M. Yoshikawa, K. Nishiyama, T. Daibou, M. Nagamine, M. Amano, S. Takahashi, M. Nakayama, N. Shimomura, H. Aikawa, S. Ikegawa, S. Yuasa, K. Yakushiji, H. Kubota, A. Fukushima, M. Oogane, T. Miyazaki, and K. Ando, in *Technical Digest – IEEE International Electron Devices Meeting* (IEEE, San Francisco, CA, USA, 2008), p. 1.
- [3] Ki Chul Chun, Hui Zhao, Jonathan D. Harms, Tae-Hyoung Kim, Jian-ping Wang, and Chris H. Kim, A scaling roadmap and performance evaluation of in-plane and perpendicular MTJ based STT-MRAMs for high-density cache memory, *IEEE J. Solid-State Circuits* **48**, 598 (2013).
- [4] Alexander Makarov, Thomas Windbacher, Viktor Sverdllov, and Siegfried Selberherr, CMOS-compatible spintronic devices: A review, *Semicond. Sci. Technol.* **31**, 113006 (2016).
- [5] S. Ikeda, K. Miura, H. Yamamoto, K. Mizunuma, H. D. Gan, M. Endo, S. Kanai, J. Hayakawa, F. Matsukura, and H. Ohno, A perpendicular-anisotropy CoFeB-MgO magnetic tunnel junction, *Nat. Mater.* **9**, 721 (2010).
- [6] D. C. Worledge, G. Hu, David W. Abraham, J. Z. Sun, P. L. Trouilloud, J. Nowak, S. Brown, M. C. Gaidis, E. J. O'Sullivan, and R. P. Robertazzi, Spin torque switching of perpendicular Ta/CoFeB/MgO-based magnetic tunnel junctions, *Appl. Phys. Lett.* **98**, 022501 (2011).
- [7] S. Bandiera, R. C. Sousa, Y. Dahmane, C. Ducruet, C. Portemont, V. Baltz, S. Auffret, I. L. Prejbeanu, and B. Dieny, Comparison of synthetic antiferromagnets and hard ferromagnets as reference layer in magnetic tunnel junctions with perpendicular magnetic anisotropy, *IEEE Magn. Lett.* **1**, 3000204 (2010).
- [8] A. Natarajarathinam, R. Zhu, P. B. Visscher, and S. Gupta, Perpendicular magnetic tunnel junctions based on thin CoFeB free layer and Co-based multilayer synthetic antiferromagnet pinned layers, *J. Appl. Phys.* **111**, 07C918 (2012).
- [9] Kay Yakushiji, Hitoshi Kubota, Akio Fukushima, and Shinji Yuasa, Perpendicular magnetic tunnel junction with enhanced anisotropy obtained by utilizing an Ir/Co interface, *Appl. Phys. Express* **9**, 13003 (2016).
- [10] M. S. Gabor, T. Petrisor, R. B. Mos, M. Nasui, C. Tiusan, and T. Petrisor, Interlayer exchange coupling in perpendicularly magnetized Pt/Co/Ir/Co/Pt structures, *J. Phys. D: Appl. Phys.* **50**, 465004 (2017).
- [11] J. Swerts, S. Mertens, T. Lin, S. Couet, Y. Tomczak, K. Sankaran, G. Pourtois, W. Kim, J. Meersschant, L. Souriau, D. Radisic, S. Van Elshocht, G. Kar, and A. Furnemont, BEOL compatible high tunnel magneto resistance perpendicular magnetic tunnel junctions using a sacrificial Mg layer as CoFeB free layer cap, *Appl. Phys. Lett.* **106**, 262407 (2015).
- [12] M. Gottwald, J. J. Kan, K. Lee, X. Zhu, C. Park, S. H. Kang, M. Gottwald, J. J. Kan, K. Lee, X. Zhu, C. Park, and S. H. Kang, Scalable and thermally robust perpendicular magnetic tunnel junctions for STT-MRAM, *Appl. Phys. Lett.* **106**, 032413 (2015).
- [13] Kay Yakushiji, Atsushi Sugihara, Akio Fukushima, Hitoshi Kubota, and Shinji Yuasa, Very strong antiferromagnetic interlayer exchange coupling with iridium spacer layer for perpendicular magnetic tunnel junctions, *Appl. Phys. Lett.* **110**, 092406 (2017).
- [14] Yiming Huai, Huadong Gan, Zihui Wang, Pengfa Xu, Xiaojie Hao, Bing K. Yen, Roger Malmhall, Nirav Pakala, Cory Wang, Jing Zhang, Yuchen Zhou, Dongha Jung, Kimihiro Satoh, Rongjun Wang, Lin Xue, and Mahendra Pakala, High performance perpendicular magnetic tunnel junction with Co/Ir interfacial anisotropy for embedded and standalone STT-MRAM applications, *Appl. Phys. Lett.* **112**, 092402 (2018).
- [15] Hiroki Koike, Takashi Ohsawa, Sadahiko Miura, Hiroaki Honjo, Shoji Ikeda, Takahiro Hanyu, Hideo Ohno, and Tetsuo Endoh, Wide operational margin capability of 1 kbit spin-transfer-torque memory array chip with 1-PMOS and 1-bottom-pin-magnetic-tunnel-junction type cell, *Jpn. J. Appl. Phys.* **53**, 04ED13 (2014).
- [16] M. Yoshikawa, E. Kitagawa, T. Nagase, T. Daibou, M. Nagamine, K. Nishiyama, T. Kishi, and H. Yoda, Tunnel magnetoresistance over 100% in MgO-based magnetic tunnel junction films with perpendicular magnetic L1₀-FePt electrodes, *IEEE Trans. Magn.* **44**, 2573 (2008).
- [17] Katayun Barmak, Bincheng Wang, Andrew T. Jesanis, David C. Berry, and Jeffrey M. Rickman, L1₀ FePt: Ordering, anisotropy constant and their relation to film composition, *IEEE Trans. Magn.* **49**, 3284 (2013).
- [18] Jaewoo Jeong, Yari Ferrante, Sergey V. Faleev, Mahesh G. Samant, Claudia Felser, and Stuart S. P. Parkin, Termination layer compensated tunnelling magnetoresistance in ferrimagnetic Heusler compounds with high perpendicular magnetic anisotropy, *Nat. Commun.* **7**, 10276 (2016).
- [19] Atsuo Ono, Kazuya Z. Suzuki, Reza Ranjbar, Atsushi Sugihara, and Shigemi Mizukami, Ultrathin films of polycrystalline MnGa alloy with perpendicular magnetic anisotropy, *Appl. Phys. Express* **10**, 023005 (2017).
- [20] Yu-Pu Wang, Sze-Ter Lim, Gu-Chang Han, and Kie-Leong Teo, High tunneling magnetoresistance ratio in perpendicular magnetic tunnel junctions using Fe-based Heusler alloys, *J. Appl. Phys.* **118**, 233906 (2015).
- [21] D. M. Bromberg, M. T. Moneck, V. M. Sokalski, J. Zhu, L. Pileggi, and J.-G. Zhu, in *Technical Digest – IEEE International Electron Devices Meeting* (IEEE, San Francisco, CA, USA, 2014), p. 33.1.1.

- [22] Shunsuke Fukami, Tetsuro Anekawa, Ayato Ohkawara, Chaoliang Zhang, and Hideo Ohno, in *Symposium on VLSI Technology, September* (IEEE, Honolulu, HI, USA, 2016), Vol. 2016, p. 1.
- [23] J. Swerts, S. Couet, E. Liu, S. Mertens, T. Lin, S. Rao, W. Kim, S. van Elshocht, A. Furnemont, and G. S. Kar, in *IEEE International Magnetism Conference (INTERMAG)* (IEEE, Dublin, Ireland, 2017), p. 1.
- [24] J. Swerts, E. Liu, S. Couet, S. Mertens, S. Rao, W. Kim, K. Garello, L. Souriau, S. Kundu, D. Crotti, F. Yasin, N. Josart, S. Sakhare, T. Devolder, S. VanBeek, B. O'Sullivan, S. Van Elshocht, A. Furnemont, and G. S. Kar, in *Technical Digest – IEEE International Electron Devices Meeting* (IEEE, San Francisco, CA, USA, 2017), p. 38.6.1.
- [25] D. C. Worledge and P. L. Trouilloud, Magnetoresistance measurement of unpatterned magnetic tunnel junction-wafers by current-in-plane tunneling, *Appl. Phys. Lett.* **83**, 84 (2003).
- [26] M. J. Donahue and D. G. Porter, OOMMF User's Guide, Version 1.0, Type Tech. Rep., Gaithersburg, MD, 1999.
- [27] E. Liu, J. Swerts, Y. C. Wu, A. Vaysset, S. Couet, S. Mertens, S. Rao, W. Kim, S. Van Elshocht, J. De Boeck, and G. S. Kar, Top-pinned STT-MRAM devices with high thermal stability hybrid free layers for high-density memory applications, *IEEE Trans. Magn.* **54**, 1 (2018).
- [28] Adrien Le Goff, Karin Garcia, Nicolas Vernier, Taiebeh Tahmasebi, Sven Cornelissen, Tai Min, and Thibaut Devolder, Effect of Ta insertion in reference layers of MTJs with perpendicular anisotropy, *IEEE Trans. Magn.* **50**, 3401704 (2014).
- [29] Adrien Le Goff, Remy Soucaille, Taiebeh Tahmasebi, Johan Swerts, Arnaud Furnemont, and Thibaut Devolder, Optimization of top-pinned perpendicular anisotropy tunnel junctions through Ta insertion, *Jpn. J. Appl. Phys.* **54**, 090302 (2015).
- [30] P. Bruno, Theory of interlayer magnetic coupling, *Phys. Rev. B* **52**, 411 (1995).
- [31] Seok Jin Yun, Sang Ho Lim, and Seong-Rae Lee, Strong interlayer exchange coupling and high post-annealing stability in perpendicularly magnetized [Pt/Co]/Ru/[Co/Pt] structures, *AIP Adv.* **6**, 025112 (2016).
- [32] Y. Iba, C. Yoshida, A. Hatada, M. Nakabayashi, A. Takahashi, Y. Yamazaki, H. Noshiro, K. Tsunoda, T. Takemura, M. Aoki, and T. Sugii, in *IEEE Symposium on VLSI Technology (VLSI)* (IEEE, Kyoto, Japan, 2013), p. T136.
- [33] Luc Thomas, Guenole Jan, Jian Zhu, Huanlong Liu, Yuan-Jen Lee, Son Le, Ru-Ying Tong, Keyu Pi, Yu-Jen Wang, Dongna Shen, Renren He, Jesmin Haq, Jeffrey Teng, Vinh Lam, Kenlin Huang, Tom Zhong, Terry Torng, and Po-Kang Wang, Perpendicular spin transfer torque magnetic random access memories with high spin torque efficiency and thermal stability for embedded applications (invited), *J. Appl. Phys.* **115**, 172615 (2014).